Mon. Not. R. Astron. Soc. **000**, 000–000 (0000) Printed 16 April 2007 (MN LATEX style file v2.2)

The 6C** sample of steep-spectrum radio sources: II – Redshift distribution and the space density of high-redshift radio galaxies

Maria J. Cruz[1,2⋆], Matt J. Jarvis[1], Steve Rawlings[1] and Katherine M. Blundell[1]

[1] *Astrophysics, Department of Physics, Keble Road, Oxford, OX1 3RH, UK*
[2] *Leiden University, Sterrewacht, Oort Gebouw, P.O. Box 9513, 2300 RA Leiden, The Netherlands*

16 April 2007

ABSTRACT

We use the 6C** sample to investigate the co-moving space density of powerful, steep-spectrum radio sources. This sample, consisting of 68 objects, has virtually complete K-band photometry and spectroscopic redshifts for 32 per cent of the sources. In order to find its complete redshift distribution, we develop a method of redshift estimation based on the $K-z$ diagram of the 3CRR, 6CE, 6C* and 7CRS radio galaxies. Based on this method, we derive redshift probability density functions for all the optically identified sources in the 6C** sample. Using a combination of spectroscopic and estimated redshifts, we select the most radio luminous sources in the sample. Their redshift distribution is then compared with the predictions of the radio luminosity function of Jarvis et al. We find that, within the uncertainties associated with the estimation method, the data are consistent with a constant co-moving space density of steep-spectrum radio sources beyond $z \gtrsim 2.5$, and rule out a steep decline.

Key words: galaxies: active - galaxies: evolution - radio continuum: galaxies - quasars: general.

1 INTRODUCTION

Powerful radio sources, such as radio galaxies and quasars, trace the most massive galaxies (Jarvis et al. 2001a; De Breuck et al. 2002; Willott et al. 2003; Zirm, Dickinson & Dey 2003) and are associated with the most massive black holes (Dunlop et al. 2003; McLure et al. 2004; McLure & Jarvis 2004) in the Universe, at all cosmic epochs. Radio galaxies have been detected up to redshifts of just above five (van Breugel et al. 1999), and quasars up to and beyond redshifts of six (Fan et al. 2003), leaving little time during which quasars and their host galaxies could form. This provides a challenge for hierarchical galaxy formation models, though some recent semi-analytic models are able to produce significant numbers of massive galaxies at high redshifts (e.g. Bower et al. 2006; Night et al. 2006). Constraining the space-density of high-redshift radio sources is therefore important, as it has implications on the theories of galaxy and structure formation. Using radio sources is also advantageous in this respect because they are selected on the basis of their radio emission and are thus free of the problems associated with optical selection methods, such as dust obscuration (cf. optically selected quasars).

It is clear that the co-moving space densities of the rarest, most powerful radio sources were much higher around $z \sim 2$ than they are at present (Longair 1966), but the form of the evolution beyond that redshift is still a matter of debate. The question of a 'redshift cut-off' (Dunlop & Peacock 1990) in the radio source population has come under careful scrutiny in recent years (Jarvis & Rawlings 2000; Jarvis et al. 2001c). The current situation is one in which there is no compelling evidence of a high-redshift decline in low-frequency selected (i.e. predominantly steep-spectrum) radio sources, whereas there is evidence for a slight decline in radio-loud quasars from high-frequency selected (i.e. predominantly flat-spectrum) samples (Dunlop & Peacock 1990, Shaver et al. 1996; Jarvis & Rawlings 2000; Wall et al. 2005).

In this study we focus on the low-frequency selected population (predominantly radio galaxies). To this effect, we use a new sample of radio sources drawn from the 151 MHz 6C survey, which has been filtered with radio criteria designed to optimize the chances of finding radio galaxies at $z > 4$. This sample, namely 6C**, has been selected to be brighter than 0.5 Jy at 151 MHz. Additional selection crite-

⋆ Email: mjc@astro.ox.ac.uk

ria have excluded all sources with radio spectral index between 151 MHz and 1.4 GHz flatter than 1, or with radio angular size larger than 13 arcsec. The final sample consists of 68 objects over an area of sky of 0.421 sr, and is statistically complete at an angular size limit of $\theta < 11$ arcsec. Full details of how the 6C** sample was selected can be found in Cruz et al. (2006, hereafter Paper I).

The selection criteria just described are similar to those of the 6C* sample (Blundell et al. 1998; Jarvis et al. 2001a,b), which was one of the samples used by Jarvis et al. (2001c) to constrain the co-moving space density of low-frequency selected radio sources. The 6C* sample was crucial in that study in sampling to high redshift ($z \simeq 4.4$). The 6C** sample, being larger (cf. 0.13 sr) and deeper (cf. $0.96 \leq S_{151} \leq 2.0$ Jy) than 6C*, aims to improve on the small-number statistics limitation of this previous work, and ultimately to extend it to higher redshifts ($z \gtrsim 5$).

Deep K-band imaging follow-up with UFTI/UIST on UKIRT, NIRI on Gemini and NIRC on Keck provided photometry for all members of the 6C** sample (Paper I). Optical spectroscopy provided redshifts for 32 per cent of the sources (Paper I and references therein). A summary of key observational information is given in Table 1.

In this paper we describe a method of redshift estimation based on the $K - z$ diagram of radio galaxies. This is presented in Section 2. In Section 3, we use the complete set of K-band magnitudes of the 6C** sample to estimate redshifts for all its optically identified members. These are compared to spectroscopic redshifts in Section 4, in order to assess the robustness of the method. The resulting estimated redshift distribution is discussed in Section 5. In Section 6 we summarize the model radio luminosity function (RLF) of Jarvis et al. (2001c). This is the most relevant model to compare our data to, because it takes into account the selection effects of the 6C* sample. In Section 7 we compare the redshift distribution (including spectroscopic redshifts) of the 6C** sample with the model predictions, and discuss the evolution of the co-moving space density of the most radio luminous, low-frequency selected sources. Unless otherwise stated, we assume throughout that $H_0 = 70$ km s^{-1}Mpc^{-1}, $\Omega_{\rm M} = 0.3$ and $\Omega_\Lambda = 0.7$. The convention used for radio spectral index is $S_\nu \propto \nu^{-\alpha}$, where S_ν is the flux-density at frequency ν.

2 REDSHIFT ESTIMATION METHOD

Infrared-photometry provides a method of redshift estimation by utilising the tightness of the relation between K-band magnitude and redshift, which is characteristic of the near-infrared Hubble diagram of radio galaxies (Lilly & Longair 1984; Eales et al. 1997; Jarvis et al. 2001a; De Breuck et al. 2002, Willott et al. 2003). The physical basis for the $K-z$ relation is not well understood. At low redshifts, the K-band emission is dominated by the old stellar population in the host galaxy; at high redshifts, K-band samples rest-frame optical wavelengths, where the star formation history can have a significant effect. Non-stellar contamination to the K-band light, in the form of reddened quasar light and/or narrow emission lines, also contributes to the difficulty of interpreting the $K - z$ diagram of radio galaxies, particularly at high redshifts ($z > 3$). Despite these caveats, the $K - z$ diagram is still of interest as a tool for redshift estimation.

Redshift estimates based on the $K-z$ diagram have generally been obtained by simple application of the empirical $K - z$ relation (e.g. Dunlop & Peacock 1990). However, the significant amount of scatter around this relation requires the use of a more sophisticated method – one which takes into account all the available information in the diagram, and also which allows us to characterise the uncertainty on the output redshift estimates. With these requirements in mind the following approach is adopted: (i) we use Monte Carlo simulations to generate a statistical universe of synthetic realisations of the $K - z$ diagram, based on a model of its underlying galaxy distribution, and (ii) we extract individual photometric redshift probability density functions from this simulated population.

2.1 The $K - z$ Diagram for the 3CRR, 6CE, 6C* and 7CRS radio galaxies

The most well defined $K - z$ diagram for radio galaxies currently available is the one obtained by Willott et al. (2003) from a combined dataset of the radio galaxies from the 3CRR (Laing, Riley & Longair 1983), 6CE (Eales et al. 1997; Rawlings, Eales & Lacy 2001), 6C* (Jarvis et al. 2001a,b) and 7CRS (Lacy et al. 2000, Willott et al. 2003) flux-limited samples. It is based on a total of 204 radio galaxies with redshifts ranging from 0.05 to 4.4, and its $K - z$ relation is well fitted by a second-order polynomial between K-magnitude and $\log_{10} z$ (Willott et al. 2003):

$$K(z) = 17.37 + 4.53 \log_{10} z - 0.31 (\log_{10} z)^2. \quad (1)$$

The main advantage of using this $K-z$ diagram is that it has been obtained from completely identified samples with close to complete, or complete redshift information. This ensures the absence of significant biases in terms of sources with the weakest lines being missed because their redshifts are difficult to obtain. Another advantage is that these samples have been selected at a similar radio-frequency to 6C**, with progressively fainter flux-density limits. The brightest sample is 3CRR selected at 178 MHz, with a flux-density limit of $S_{178} \geq 10.9$ Jy ($S_{151} \geq 12.4$ Jy, assuming a spectral index of 0.8); the faintest sample is 7CRS selected at 151 MHz, with a flux-density limit of $S_{151} \geq 0.5$ Jy. The intermediate samples are 6CE and 6C* selected at 151 MHz, with flux-density limits of $2.0 \leq S_{151} \leq 3.93$ Jy and $0.96 \leq S_{151} \leq 2.00$ Jy, respectively. This results in a wide range in radio luminosity, which has made the investigation of the radio-luminosity dependence of the $K - z$ relation possible in an unprecedented way. The correlation between K-band luminosity and radio luminosity has been one of the major worries with redshift estimates based on the $K - z$ relation.

Willott et al. (2003) found a statistically significant mean luminosity difference between the 3CRR and 7CRS radio galaxies of 0.55 mag in K-band, over all redshifts. However, the 6C radio galaxies were found to differ on average from the 3C ones by only $\simeq 0.3$ mag, which is much smaller than the value ($\simeq 0.6$ mag) reported previously (Eales et al. 1997). The mean luminosity difference between the 6C and 7C galaxies was not found to be significant. These results are confirmed by McLure et al. (2004), who used HST data to study the host galaxy properties of a sample of radio

(1) Source	(2) S_{151}	(3) α_{151}^{1400}	(4) K	(5) z	(6) Line	(7) $\log_{10} L_{\rm line}$	(8) Ref.
6C**0714+4616	1.65	1.25	16.316(8)	1.466	CIV	36.05	Cea
6C**0717+5121	1.24	1.11	17.788(5)	nd			
6C**0726+4938	0.61	1.19	18.168(8)	1.203?	[O II]?	35.15	Cea
6C**0737+5618	0.74	1.28	$>$ 21.1(8)	nd			
6C**0744+3702	0.64	1.31	19.440(8)	2.992	Lyα	35.78	DBea
6C**0746+5445	0.53	1.04	18.423(3)	2.156	Lyα	–	Cea
6C**0754+4640	0.69	1.07	19.971(5)	nd			
6C**0754+5019	1.05	1.07	20.629(5)	2.996	Lyα	35.81	Cea
6C**0801+4903	1.08	1.13	19.855(5)				
6C**0810+4605	10.26	1.01	15.993(8)	0.620	[O II]	36.17	Cea
6C**0813+3725	0.50	1.24	18.798(8)	nd			
6C**0824+5344	0.88	1.06	19.392(8)	2.824	Lyα	36.94	Cea
6C**0829+3902	0.51	1.16	19.413(5)	nd			
6C**0832+4420	0.52	1.14	18.915(8)				
6C**0832+5443	0.60	1.02	19.283(5)	3.341	Lyα	36.68	Cea
6C**0834+4129	0.50	1.00	19.378(8)	2.442	Lyα	36.35	Cea
6C**0848+4803	0.71	1.26	17.828(8)				
6C**0848+4927	0.94	1.03	18.222(8)	nd			
6C**0849+4658	3.50	1.03	17.319(8)				
6C**0854+3500	0.87	1.06	18.121(8)	2.382	Lyα	–	Cea
6C**0855+4428	0.94	1.06	18.485(5)				
6C**0856+4313	0.59	1.00	17.999(8)	1.761	Lyα	36.44	Cea
6C**0902+3827	1.60	1.04	19.290(5)	nd			
6C**0903+4251	3.14	1.08	16.615(8)	0.907	[O II]	35.20	McC
6C**0909+4317	3.36	1.01	18.635(8)				
6C**0912+3913	0.56	1.02	17.595(8)				
6C**0920+5308	0.56	1.03	14.526(8)				
6C**0922+4216	2.70	1.06	15.928(8)	1.750			Vea
6C**0924+4933	0.93	1.05	14.955(8)				
6C**0925+4155	0.91	1.01	20.279(5)	nd			
6C**0928+4203	2.04	1.22	18.448(8)	1.664	Lyα	36.95	Cea
6C**0928+5557	0.58	1.04	17.285(5)				
6C**0930+4856	0.66	1.02	18.903(8)				
6C**0935+4348	1.09	1.36	$>$ 20.9(8)	2.321?	Lyα?	36.70	Cea
6C**0935+5548	0.90	1.01	18.325(8)				
6C**0938+3801	1.03	1.13	18.132(8)	nd			
6C**0943+4034	0.99	1.06	17.592(8)				
6C**0944+3946	0.66	1.00	19.088(8)				
6C**0956+4735	6.13	1.13	17.192(8)	1.026	[O II]	35.75	McC
6C**0957+3955	0.62	1.01	18.264(8)				
6C**1003+4827	6.88	1.09	16.950(8)				
6C**1004+4531	0.70	1.01	17.183(8)				
6C**1006+4135	0.52	1.01	19.825(5)				
6C**1009+4327	2.89	1.23	20.513(3)	1.956	Lyα	35.64	Cea
6C**1015+5334	1.44	1.05	18.516(8)				
6C**1017+3436	1.17	1.04	18.972(8)				
6C**1018+4000	0.53	1.02	18.434(8)				
6C**1035+4245	1.89	1.28	17.250(8)				
6C**1036+4721	3.70	1.03	16.967(8)	1.758	Lyα	–	Cea
6C**1043+3714	2.62	1.04	17.579(3)	0.789			ASea
6C**1044+4938	1.66	1.08	18.685(5)				
6C**1045+4459	0.95	1.11	18.438(5)	2.571	Lyα	36.55	Cea
6C**1048+4434	1.51	1.02	18.628(5)				
6C**1050+5440	0.93	1.20	19.715(8)	nd			
6C**1052+4349	0.51	1.03	17.081(8)				
6C**1056+5730	2.66	1.12	17.295(8)				
6C**1100+4417	0.72	1.09	18.095(8)				
6C**1102+4329	1.11	1.08	19.661(8)	2.734	Lyα	36.62	Cea
6C**1103+5352	2.67	1.03	20.142(5)				
6C**1105+4454	0.83	1.01	17.729(8)				
6C**1106+5301	0.77	1.13	17.354(8)				
6C**1112+4133	0.54	1.33	18.044(8)				
6C**1125+5548	0.63	1.23	19.680(5)				
6C**1132+3209	0.63	1.04	14.505(3)	0.231			Bea
6C**1135+5122	0.66	1.10	18.554(5)				

(1) Source	(2) S_{151}	(3) α_{151}^{1400}	(4) K	(5) z	(6) Line	(7) $\log_{10} L_{\rm line}$	(8) Ref.
6C**1138+3309	0.93	1.22	18.014(8)				
6C**1138+3803	0.51	1.05	17.351(3)				
6C**1149+3509	0.61	1.06	18.729(8)				

Table 1. Summary of the observational data on the 6C** sample. **Column 1:** Name of the 6C** source. **Column 2:** 151 MHz flux-density measurements in Jy from the 6C survey (Hales et al. 1988; Hales et al. 1990). **Column 3:** Radio spectral index evaluated between 151 MHz and 1.4 GHz from the 6C and NRAO VLA SKy Survey (NVSS; Condon et al. 1998) flux densities. **Column 4:** K-band magnitude within the angular aperture in arcsec given in brackets. **Column 5:** Redshift: '?' signifies that this value is uncertain, 'nd' signifies that the source was observed but there were no emission lines and/or continuum detected. **Column 6:** Prominent emission line in the existing spectra, '?' signifies that the line identification is uncertain. **Column 7:** $\log_{10}$ of the luminosity of the line listed in Column 6 (measured in units of W): '–' signifies that the data were inadequate to obtain a line luminosity, due to the absence of a spectrophotometric standard or non-photometric observing conditions. **Column 8:** Reference for the redshift of the source, Cea = Cruz et al. (2006), DBea = De Breuck et al. (2001), McC = McCarthy (1991), Vea = Vigotti et al. (1990), ASea = Allington-Smith et al. (1985), Bea = Brinkmann et al. (2000).

galaxies at $0.4 \leq z \leq 0.6$, which spans three decades in radio luminosity. They found mean luminosity differences in the R-band of $\simeq 0.3$ mag between the 3C and 6C samples, and $\simeq 0.8$ mag between the 3C and 7C samples[1]. These results are in good quantitative agreement with those of Willott et al. (2003). From both studies it follows that there is a correlation between radio luminosity and host luminosity within the 3CRR, 6CE and 7CRS samples. This has been interpreted as suggestive of a correlation of both these properties with black hole mass (Willott et al. 2003; McLure et al. 2004). However, the weakness of these correlations means that the radio galaxies within the combined dataset used by Willott et al. (2003) follow essentially the same $K-z$ relation.

2.2 Parametric modelling of the $K-z$ Diagram

In this section we consider how to model the distribution of galaxies in the $K-z$ diagram. We start from the combined dataset of radio galaxies from the 3CRR, 6CE, 6C* and 7CRS samples[2], and fit their distribution in $\log_{10} z$ with a function of the form:

$$n(z) = A \exp\left\{ -\left[\sum_{i=0}^{n} a_i \, (\log_{10}\, z)^i\right]^2\right\}, \qquad (2)$$

where A and a_i are free parameters. The histogram of the distribution in $\log_{10} z$ along with the best-fitting function are shown in Fig. 1. We use a fifth order polynomial as the argument to the exponential, and find the best-fitting coefficients to be:

$$A = 197.96; \quad a_0 = -0.39; \quad a_2 = 1.00; \quad a_4 = 1.47;$$
$$a_1 = \ \ 1.17; \quad a_3 = 1.83; \quad a_5 = 0.38.$$

For any given value of redshift z, we assume that $n(z)$ of the sources follow a Gaussian distribution in K-band magnitude about a mean value $k(z)$, given by the $K-z$ relation (Eq. 1) at that redshift, i.e.:

[1] These magnitude differences were measured in the I-band and converted to the R-band assuming a constant $R-I$ colour (McLure et al. 2004).

[2] These data can be obtained on-line at http://www-astro.physics.ox.ac.uk/∼cjw/kz/kz.html

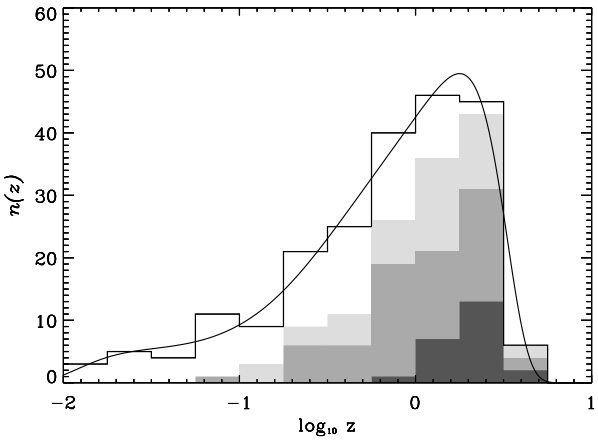

Figure 1. Histogram of the distribution in $\log_{10} z$ of the radio galaxies in the 3CRR, 6CE, 6C* and 7CRS samples. The bin width is $\Delta(\log_{10} z) = 0.25$. The white regions correspond to 3CRR sources, the light shaded regions to 6CE sources, the intermediate shaded regions are the 7CRS sources, and the dark shaded regions the 6C* sources. The solid line represents the best-fitting function to the data – $n(z) \times \Delta(\log_{10} z)$ – given by Eq. 2 and the coefficients in the text.

$$\rho(K|z) = \frac{n(z)}{\sigma_K \sqrt{2\pi}} \ \exp\left\{-\frac{[K-k(z)]^2}{2(\sigma_K)^2}\right\}, \qquad (3)$$

where K is the aperture- and emission-line corrected K-band magnitude measured for any given source (as described in Jarvis et al. 2001a; Willott et al. 2003) and σ_K, the dispersion, is independent of redshift. This assumption is motivated by the results of Willott et al. (2003), who evaluated the dispersion about the best-fitting $K-z$ relation as a function of redshift. They found no significant increase up to $z = 3$, which is also in agreement with the results of Jarvis et al. (2001a).

In order to constrain the free-parameter σ_K we follow the maximum likelihood formulation of Marshall et al. (1983). Defining S as $-2\ln\mathcal{L}$, where $\mathcal{L}$ is the likelihood function, the best-fit parameter is obtained by minimizing the value of S, which in our case is given by:

$$S = -2\sum_{i=1}^{N} \ln[\rho(K_i|z_i)] + 2\int\int \rho(K|z)\mathrm{d}K\,\mathrm{d}(\log_{10}\,z). \quad (4)$$

In the first term the sum is over all N radio galaxies in the combined sample; the second term is the integral of the model distribution being tested and should give $\approx 2N$ for good fits. The upper and lower limits of the integral are: $10.0 \leq K \leq 21.0$ and $-1.3 \leq \log_{10} z \leq 1.0$ (corresponding to $0.05 \leq z \leq 10$). To find the best-fitting parameter we evaluated S over a range of $0.01 \leq \sigma_K \leq 1$. We found a minimum value of S for $\sigma_K = 0.593 \pm 0.02$ mag. This value is in good quantitative agreement with the results of Willott et al. (2003), who found a scatter of 0.58 mag in the $K-z$ relation at all redshifts up to $z = 3$.

2.3 Redshift probability distributions from the simulated $K-z$ diagram

Adopting the model described in the previous section, such that $\rho(K|z)\,\mathrm{d}K\,\mathrm{d}(\log_{10} z)$ is the expected number of sources in the differential magnitude element $\mathrm{d}K$ and in the differential redshift element $\mathrm{d}(\log_{10} z)$, and using Poisson probabilities, we use Monte Carlo simulations to generate a large number of samples that mimic the combined 3CRR/6CE/6C*/7CRS dataset. We combine all the simulated datasets to construct a highly populated synthetic $K-z$ diagram from which it is possible to extract photometric redshift probability density functions for any given value of K-magnitude. We extract these functions from a total of 10000 simulated samples, i.e. from a $K-z$ diagram with ~ 2 million sources.

The probability density functions $p(z|K)$ can be obtained for any given source with $10 \leq K \leq 21$ by taking the points along the horizontal band on the synthetic $K-z$ diagram defined by $[K-\Delta K/2; K+\Delta K/2]$, where K is the K-band magnitude measured for that source and ΔK an appropriately small number, and by fitting the values of the relative frequency of each data point along this band. For any such source these values are best-fit by a $\log_{10}$-normal distribution of the random variable z with probability density function:

$$p(z|K) = \frac{1}{\ln(10)\,z\,\sqrt{2\pi\sigma^2}} \exp\left\{-\frac{[\log_{10}(z)-\mu]^2}{2\,\sigma^2}\right\} \quad (5)$$

where μ and σ are the mean and standard deviation of the distribution for the normal random variable $\log_{10} z$. The best-fitting estimate for z is thus defined as:

$$z_{\rm est} = 10^{\mu}, \quad (6)$$

and the asymmetric 68% confidence interval as:

$$10^{\mu-\sigma} \leq z_{\rm est} \leq 10^{\mu+\sigma}. \quad (7)$$

3 RESULTS

Using K-band photometry from Paper I, we extract photometric redshift probability density functions for all the identified sources in the 6C** sample[3]. In Table 2 we quote the values for the best-fitting redshift estimates $z_{\rm est}$ and 68% confidence intervals (C.I.), along with the p.d.f parameters σ and μ, and the K-band magnitudes used to extract them. In Fig. 2 we present the probability density functions $p(z|K)$ for the 21 identified sources which have spectroscopic redshifts[4] (Paper I and the references in Table 2). We note that there is in general good agreement between the redshift estimates and the spectroscopic redshifts. The notable exceptions are the quasars, which have systematically low estimated redshifts because of the incorrect underlying assumption that the K-band light is dominated by starlight.

Where possible we have used K-magnitudes measured in an 8-arcsec diameter aperture to extract the probability density functions. For sources which do not have K-band magnitudes measured in an 8-arcsec diameter aperture, due to the presence of a nearby object (Paper I), we have used those measured in 3- or 5-arcsec diameter apertures, and applied an empirical correction of -0.21 and -0.41 mag, respectively. These values have been derived from the median difference between the small- (3 or 5 arcsec) and large-aperture (8 arcsec) magnitudes (presented in table 5 of Paper I). This choice of aperture and these corrections were designed to minimize the effects of the absence of an aperture correction in our analysis.

We recall that the $K-z$ diagram we use in our modelling is defined in terms of the aperture- and emission-line corrected K-band magnitudes. The aperture and emission-line corrections can only be obtained upon a priori knowledge of redshift and are thereby not available to us in this analysis. In the remainder of this section we will discuss how the absence of these corrections affects our redshift estimates.

3.1 Aperture correction

The aperture correction, e.g. as prescribed by Eales et al. (1997), involves converting the apparent angular size aperture magnitudes to standard 63.9 kpc metric apertures. This value was chosen because it corresponds to ≈ 8 arcsec at $z > 1$ for a $H_0 = 50\,\mathrm{km\,s^{-1}\,Mpc^{-1}}$, $\Omega_{\rm M} = 1$ and $\Omega_\Lambda = 0$ cosmology. As it is immediately apparent from Fig. 3, aperture corrections are generally very small and for $z > 0.6$ not strongly dependent on redshift. For the samples used in our modelling, at $z > 0.6$ magnitudes measured in 8-arcsec apertures have aperture corrections which are less than ± 0.05 mag. For the magnitudes measured in 5- and 3-arcsec apertures, the values of the aperture correction are very similar to the empirical corrections we apply to our data. For these reasons, and for the high-redshift objects which we are most interested in, we consider the absence of an aperture correction on a source-to-source basis has a negligible effect on our redshift estimates.

[3] We exclude just two sources: 6C**0737+5618 and 6C**0935+4348. Both are not identified in K-band down to a 3σ limiting magnitude of $K \sim 21$ in an 8-arcsec diameter aperture (Paper I). Therefore, we do not extract probability density functions for these sources, as the $K-z$ diagram of radio galaxies is not well defined for $K > 21$ (see also the caption of Table 2).

[4] This excludes 6C**0935+4348, which has uncertain K-band identification and redshift. This source is discussed further in Paper I.

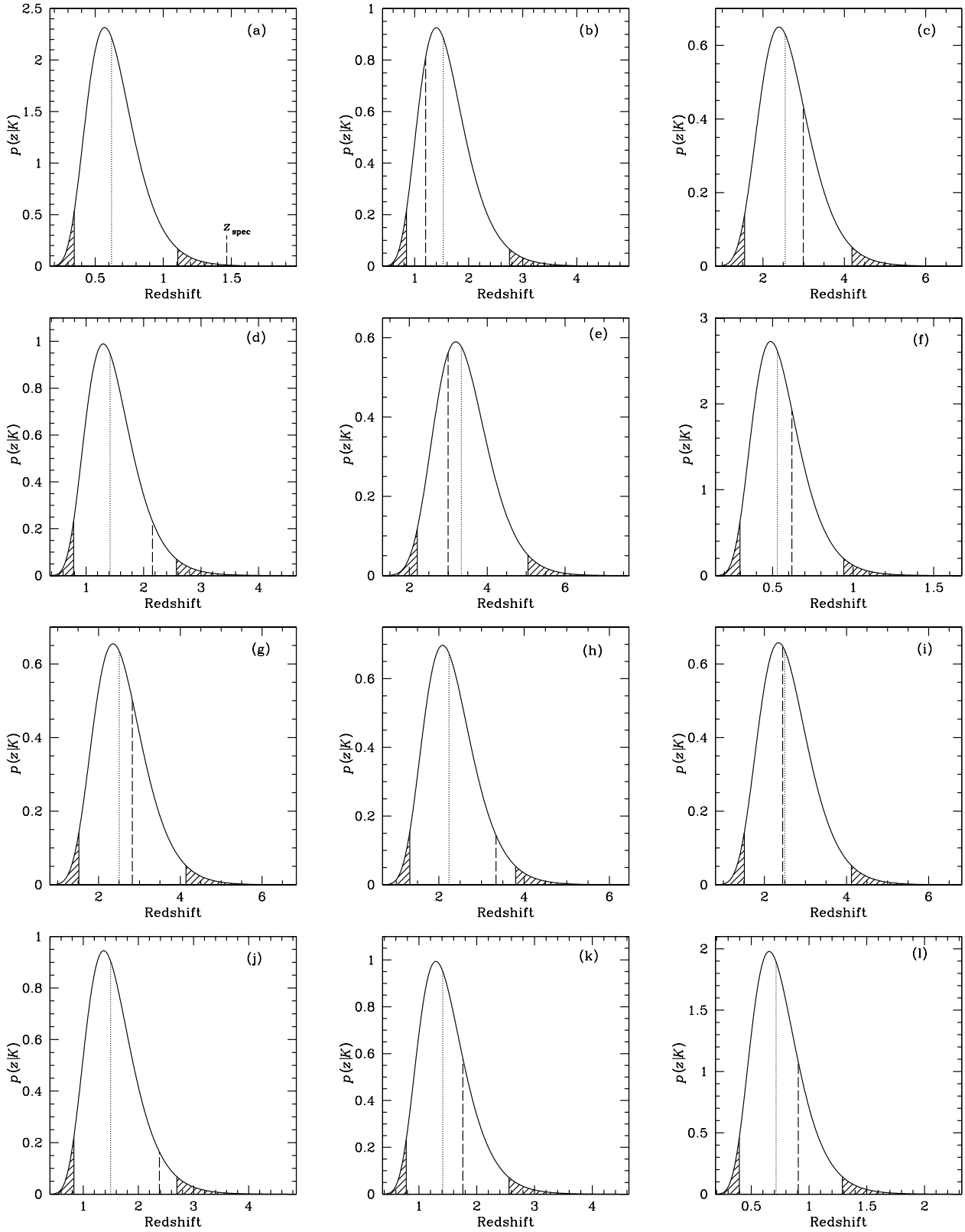

Figure 2. The redshift probability density functions $p(z|K)$ for the 21 (identified) 6C** sources which have spectroscopic redshifts, normalised such that the area under the curve is unity. For each graph: the unshaded region corresponds to the 95% confidence interval; dotted lines show the location of the redshift estimate; dashed lines the location of the measured spectroscopic redshift. In some cases, where the spectroscopic redshift line is difficult to visualise, we add the label $z_{\rm spec}$. (a) **6C**0714+4616** (quasar); (b) **6C**0726+4938**; (c) **6C**0744+3702**; (d) **6C**0746+5445**; (e) **6C**0754+5019**; (f) **6C**0810+4605**; (g) **6C**0824+5344**; (h) **6C**0832+5443**; (i) **6C**0834+4129** (j) **6C**0854+3500**; (k) **6C**0856+4313**; (l) **6C**0903+4251**;

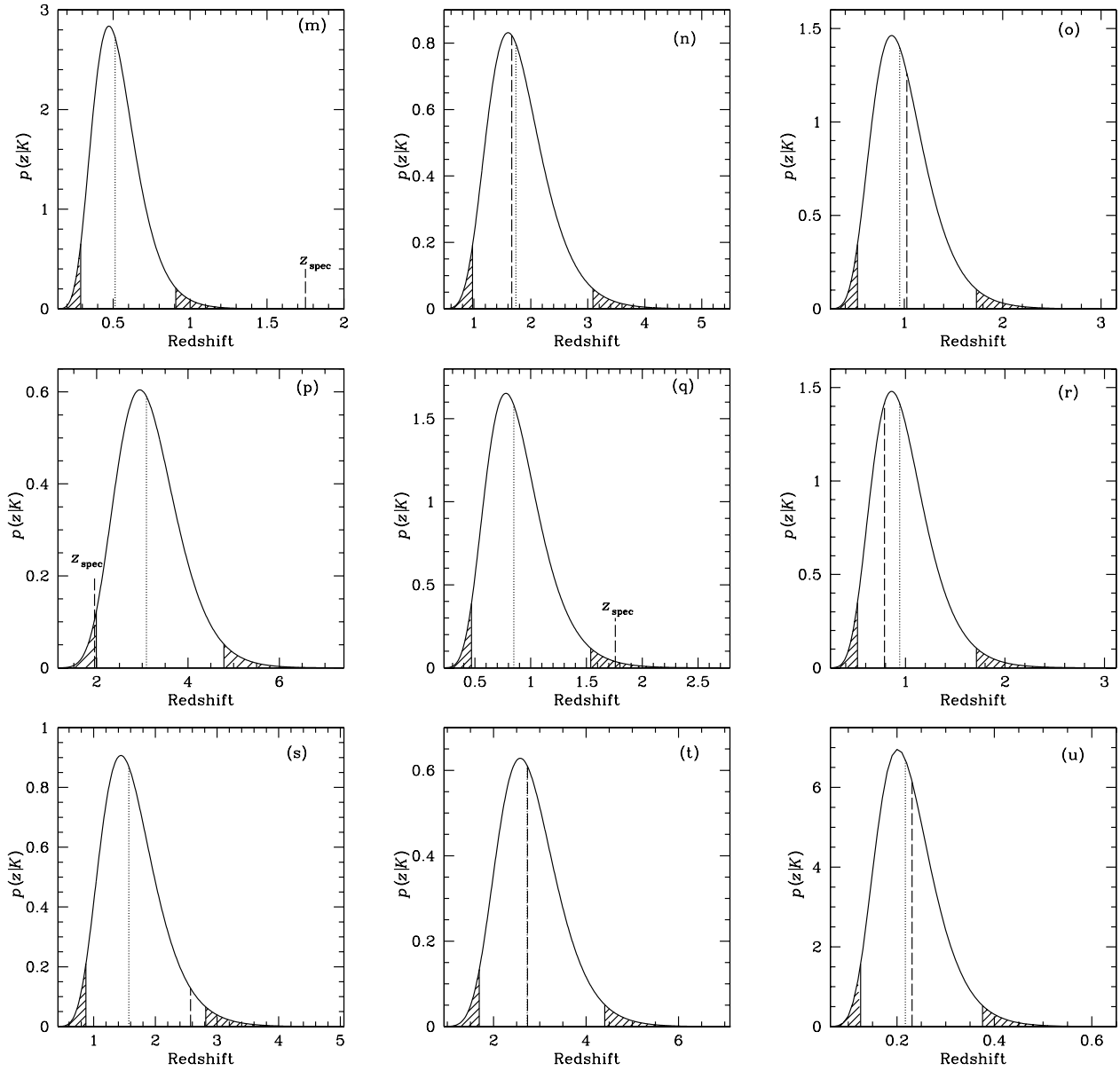

Figure 2. continued: (m) **6C**0922+4933** (quasar); (n) **6C**0928+4203** (quasar); (o) **6C**0956+4735**; (p) **6C**1009+4327**; (q) **6C**1036+4721** (quasar); (r) **6C**1043+3714**; (s) **6C**1045+4459**; (t) **6C**1102+4329**; (u) **6C**1132+3209**.

3.2 Emission line contribution

Emission line contribution to the K-band magnitudes can be significant at $z > 2$, when the strong Hα 6583, [O III] 5007 and [O II] 3727 emission lines are redshifted into the K-band at $1.9 \lesssim z \lesssim 2.7$, $2.9 \lesssim z \lesssim 3.7$ and $4.2 \lesssim z \lesssim 5.2$, respectively (Eales & Rawlings 1993, 1996; Jarvis et al. 2001a). The emission line correction, prescribed by Jarvis et al. (2001a), takes into account the [O II] emission-line-radio luminosity correlation of Willott (2001), and the emission-line flux ratios from McCarthy (1993) to determine the contribution to the K-band magnitude from all the emission lines at a given redshift. The emission line correction is therefore dependent both on radio luminosity and on redshift, but more strongly on redshift. This strong dependency is visible in Fig. 4, where we plot the emission line correction as a function of redshift for the radio galaxies in the 3CRR, 6CE, 6C* and 7CRS samples. However, it can be seen that, apart from one of the sources which has an emission line correction of 0.65 mag, all the sources in this dataset have emission line corrections which are smaller than the scatter in the $K - z$ diagram. Therefore, we expect some of the most radio luminous sources in 6C**, which are at $z > 2$ to have an additional systematic uncertainty in their redshift estimates, due to emission line contamination to their K-band magnitudes. These will have redshift estimates, based on our method, which are biased towards lower values. This is a consequence of the contribution from bright emission lines, which make the objects brighter (in K-band).

Source	K	μ	σ	$z_{\rm est}$	68% C.I.	$z_{\rm spectr}$	$\log_{10} L_{151}$ est.	$\log_{10} L_{151}$ spec.
6C**0714+4616	16.316	-0.208	0.126	0.619	[0.463, 0.827]	1.466	26.38	27.34
6C**0717+5121	17.575	0.061	0.130	1.150	[0.851, 1.553]		26.90	
6C**0726+4938	18.168	0.184	0.128	1.529	[1.139, 2.053]	1.203?	26.94	26.67
6C**0737+5618	>21.1			> 4.0			>28.18	
6C**0744+3702	19.440	0.406	0.108	2.549	[1.986, 3.273]	2.992	27.60	27.78
6C**0746+5445	18.011	0.152	0.129	1.421	[1.056, 1.911]	2.156	26.74	27.18
6C**0754+4640	19.758	0.449	0.102	2.810	[2.222, 3.555]		27.60	
6C**0754+5019	20.416	0.523	0.090	3.331	[2.709, 4.097]	2.996	27.97	27.85
6C**0801+4903	19.645	0.435	0.104	2.722	[2.143, 3.459]		27.79	
6C**0810+4605	15.993	-0.276	0.125	0.529	[0.397, 0.706]	0.620	26.96	27.12
6C**0813+3725	18.798	0.305	0.120	2.016	[1.530, 2.658]		27.18	
6C**0824+5344	19.392	0.399	0.109	2.507	[1.950, 3.223]	2.824	27.58	27.71
6C**0829+3902	19.200	0.371	0.113	2.350	[1.813, 3.045]		27.32	
6C**0832+4420	18.915	0.324	0.118	2.110	[1.607, 2.771]		27.20	
6C**0832+5443	19.070	0.350	0.115	2.240	[1.717, 2.922]	3.341	27.27	27.69
6C**0834+4129	19.378	0.397	0.109	2.496	[1.941, 3.211]	2.442	27.29	27.27
6C**0848+4803	17.828	0.114	0.130	1.300	[0.964, 1.754]		26.85	
6C**0848+4927	18.222	0.195	0.127	1.567	[1.168, 2.102]		27.09	
6C**0849+4658	17.319	0.0056	0.130	1.013	[0.751, 1.366]		27.18	
6C**0854+3500	18.121	0.175	0.128	1.496	[1.113, 2.011]	2.382	27.02	27.52
6C**0855+4428	18.272	0.205	0.127	1.604	[1.197, 2.150]		27.12	
6C**0856+4313	17.999	0.150	0.129	1.413	[1.050, 1.901]	1.761	26.76	27.00
6C**0902+3827	19.077	0.351	0.115	2.246	[1.723, 2.927]		27.71	
6C**0903+4251	16.615	-0.146	0.128	0.715	[0.532, 0.961]	0.907	26.78	27.03
6C**0909+4317	18.635	0.274	0.122	1.881	[1.420, 2.493]		27.83	
6C**0912+3913	17.595	0.065	0.131	1.162	[0.860, 1.570]		26.53	
6C**0920+5308	14.526	-0.576	0.121	0.265	[0.201, 0.351]		24.99	
6C**0922+4216	15.928	-0.290	0.124	0.512	[0.385, 0.682]	1.750	26.35	27.67
6C**0924+4933	14.955	-0.490	0.122	0.324	[0.244, 0.429]		25.41	
6C**0925+4155	20.069	0.486	0.098	3.060	[2.444, 3.831]		27.77	
6C**0928+4203	18.448	0.240	0.125	1.736	[1.302, 2.315]	1.664	27.62	27.57
6C**0928+5557	17.072	-0.048	0.130	0.896	[0.664, 1.208]		26.28	
6C**0930+4856	18.903	0.322	0.118	2.100	[1.599, 2.759]		27.24	
6C**0935+4348	>20.9			> 4.0		2.321?	>28.38	27.75
6C**0935+5548	18.325	0.216	0.126	1.644	[1.229, 2.199]		27.11	
6C**0938+3801	18.132	0.177	0.128	1.504	[1.119, 2.021]		27.12	
6C**0943+4034	17.592	0.064	0.131	1.160	[0.858, 1.567]		26.79	
6C**0944+3946	19.088	0.353	0.115	2.253	[1.729, 2.936]		27.31	
6C**0956+4735	17.192	-0.021	0.130	0.952	[0.706, 1.284]	1.026	27.39	27.47
6C**0957+3955	18.264	0.204	0.127	1.599	[1.193, 2.143]		26.92	
6C**1003+4827	16.950	-0.074	0.129	0.842	[0.626, 1.133]		27.30	
6C**1004+4531	17.183	-0.023	0.130	0.948	[0.703, 1.278]		26.41	
6C**1006+4135	19.612	0.430	0.104	2.691	[2.115, 3.423]		27.40	
6C**1009+4327	20.101	0.490	0.095	3.089	[2.479, 3.850]	1.956	28.42	27.91
6C**1015+5334	18.516	0.253	0.124	1.790	[1.344, 2.383]		27.42	
6C**1017+3436	18.972	0.334	0.117	2.157	[1.647, 2.824]		27.53	
6C**1018+4000	18.434	0.237	0.125	1.725	[1.292, 2.303]		26.94	
6C**1035+4245	17.250	-0.0089	0.130	0.980	[0.727, 1.320]		26.96	
6C**1036+4721	16.967	-0.071	0.129	0.849	[0.631, 1.143]	1.758	27.02	27.81
6C**1043+3714	17.167	-0.026	0.130	0.941	[0.698, 1.268]	0.789	26.98	26.79
6C**1044+4938	18.472	0.244	0.125	1.754	[1.317, 2.338]		27.48	
6C**1045+4459	18.225	0.196	0.127	1.569	[1.170, 2.105]	2.571	27.12	27.66
6C**1048+4434	19.415	0.233	0.125	1.711	[1.282, 2.284]		27.38	
6C**1050+5440	19.715	0.443	0.103	2.773	[2.188, 3.516]		27.79	

Source	K	μ	σ	$z_{\rm est}$	68% C.I.	$z_{\rm spectr}$	$\log_{10} L_{151}$ est.	spec.
6C**1052+4349	17.081	-0.046	0.130	0.900	[0.667, 1.213]		26.22	
6C**1056+5730	17.295	0.00073	0.130	1.002	[0.743, 1.351]		27.09	
6C**1100+4417	18.095	0.170	0.128	1.478	[1.100, 1.987]		26.93	
6C**1102+4329	19.661	0.436	0.104	2.732	[2.150, 3.472]	2.734	27.78	27.79
6C**1103+5352	19.929	0.469	0.098	2.947	[2.350, 3.695]		28.21	
6C**1105+4454	17.729	0.092	0.129	1.237	[0.918, 1.667]		26.77	
6C**1106+5301	17.354	0.013	0.130	1.030	[0.764, 1.390]		26.58	
6C**1112+4133	18.044	0.159	0.129	1.443	[1.073, 1.941]		26.87	
6C**1125+5548	19.467	0.410	0.108	2.570	[2.005, 3.295]		27.55	
6C**1132+3209	14.093	-0.663	0.119	0.217	[0.165, 0.286]	0.231	24.84	24.90
6C**1135+5122	18.341	0.219	0.126	1.656	[1.239, 2.215]		27.02	
6C**1138+3309	18.014	0.153	0.129	1.423	[1.058, 1.914]		27.05	
6C**1138+3803	16.939	-0.077	0.129	0.838	[0.623, 1.127]		26.15	
6C**1149+3509	18.729	0.292	0.121	1.958	[1.482, 2.588]		27.15	

Table 2. Redshift estimates for all the members of the 6C** sample. Column one lists the source names. Column two lists the K-band magnitudes measured in, or corrected to an 8-arcsec diameter aperture (see Section 3). Columns three and four list the probability density function (Eq. 5) parameters μ and σ, respectively. Column five lists the redshift estimates as obtained through Eq. 6. Column six lists the 68% confidence intervals as defined in Eq. 7. Column seven lists the spectroscopic redshifts (references as in Table 1). Columns eight and nine list the rest-frame 151 MHz radio luminosities (measured in units of W Hz^{-1} sr^{-1} and calculated assuming a power-law spectral index) based on the estimated and spectroscopic redshifts, respectively. Note: 6C**0737+5618 and 6C**0935+4348 are not identified in K-band down to a 3σ limiting magnitude of $K \sim 21$ mag in a 8-arcsec diameter aperture (Paper I). Therefore, we do not extract probability density functions for these sources. We give lower limits for their redshift estimates, although we caution that they have been determined by extrapolation of our method to $K \gtrsim 21$ mag, where the $K-z$ diagram is not well-defined.

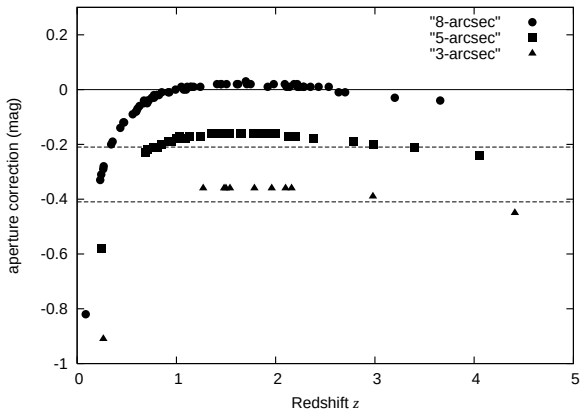

Figure 3. The aperture corrections applied to the K-band magnitudes measured in 8-arcsec (filled circles), 5-arcsec (filled boxes) and 3-arcsec (filled triangles) diameter apertures for the radio galaxies in the 3CRR, 6CE, 6C* and 7CRS samples as a function of redshift. The dashed lines correspond to the empirical corrections applied to the 6C** sources (see Section 3) of -0.21 mag (for magnitudes measured in 5-arcsec apertures) and -0.41 mag (for magnitudes measured in 3-arcsec apertures).

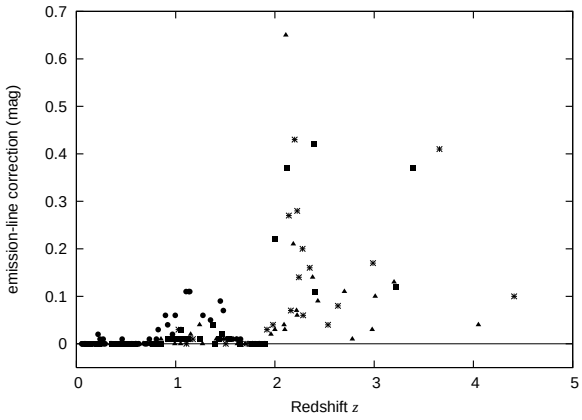

Figure 4. The emission line corrections applied to the K-band magnitudes (after aperture correction) of the radio galaxies in the 3CRR (filled circles), 6CE (filled boxes), 6C* (stars) and 7CRS (filled triangles) samples as a function of redshift.

4 COMPARISON WITH SPECTROSCOPIC REDSHIFTS

In Fig. 5 we plot redshift estimates against spectroscopic redshifts for the 6C** sample. It is apparent that the majority of sources lie under the line of equality between estimated and spectroscopic redshifts, implying a bias towards redshift under-estimation. This is not unexpected given the level of spectroscopic incompleteness of the sample. The subset of sources for which we have spectroscopic redshifts is biased towards sources which have strong emission lines and for which spectroscopy is easier to obtain. Depending on their redshift, these are more likely to be the sources in which emission line contamination to the K-band light is more significant. Indeed, if we exclude the quasars, it can be seen that the sources which show larger deviations from the

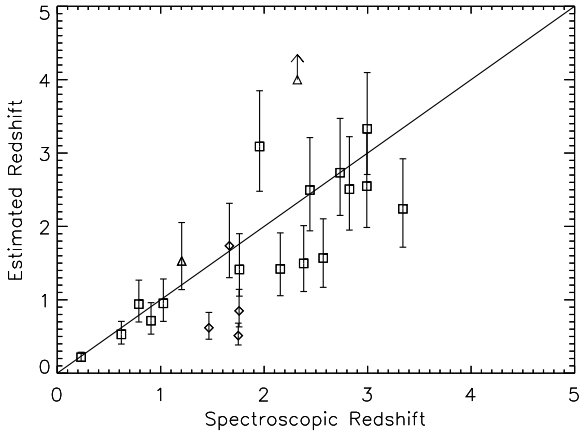

Figure 5. Comparison of estimated and spectroscopic redshifts for 6C** sources. The error bars show the asymmetric 68% confidence interval about the best-fitting redshift estimate. The solid line is the $z_{\rm est} = z_{\rm spec}$ line. Triangles represent the sources with uncertain redshifts, boxes the sources with secure redshifts, and diamonds the quasars. The triangle with an upward arrow represents the lower limit estimate for 6C**0935+4348 (see also the caption of Table 2).

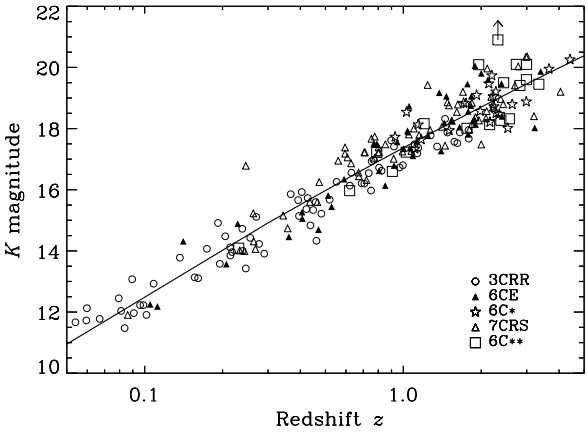

Figure 6. $K - z$ diagram of radio galaxies. The new spectroscopically confirmed 6C** data are plotted along with the 3CRR, 6CE, 6C* and 7CRS. The solid line is the $K-z$ relation of Willott et al. (2003). 6C**0935+4348, the major 6C** $K - z$outlier, is represented by a box with an upward arraw, since this is also a K-magnitude lower limit.

equality line are in excess at $z > 2$. As we have discussed in Section 3.2, this is consistent with an unaccounted-for emission line contribution which systematically biases some of the sources towards lower redshifts. However, as it is clear from Fig. 2, the deviations are in all of the cases – 6C**0746+5445 ($z_{\rm spec} = 2.156$, Fig. 2d); 6C**0832+5443 ($z_{\rm spec} = 3.341$, Fig. 2h); 6C**0854+3500 ($z_{\rm spec} = 2.382$, Fig. 2j) and 6C**1045+4459 ($z_{\rm spec} = 2.571$, Fig. 2s) – within the 95% confidence interval upper-bound.

Not surprisingly, the quasars as a whole show the largest deviations from the $z_{\rm est} = z_{\rm spec}$ line. The $K-z$ diagram does not hold for these objects and therefore their K-band magnitudes make poor redshift estimators. Quasars can have a strong contribution to their K-band light by the non-stellar continuum produced by the AGN. For this reason, any attempted estimates via the $K - z$ diagram will be invariably much lower than the true redshift. This is particularly clear in Fig. 2 (a,m,q), where it can be seen that the estimates deviate by more than 2σ, and in one case (6C**0922+4216) more than 3σ, from the true redshift. We note, however, that the redshift of one of the quasars (6C**0928+4203 with $z_{\rm spec} = 1.664$, Fig. 2n) is accurately estimated with our method. Possibly because its broad Mg II emission is the result of scattered light from the broad line region and the nucleus is heavily obscured (Paper I).

Two sources have photometric redshifts which are significantly overestimated by our method. One is 6C**1009+4327 ($z_{\rm spec} = 1.956$, $z_{\rm est} = 3.089$), which is a very faint source ($K = 20.5$ mag in a 3-arcsec aperture) with spectrum showing weak Lyman-α emission. The other is 6C**0935+4348 ($z_{\rm spec} = 2.321$, $z_{\rm est} > 4.0$), which is one of the faintest sources in the sample, with $K > 21.7$ mag in a 3-arcsec aperture. This source is two magnitudes fainter than the mean $K - z$ relation, which makes it a substantial $K - z$ outlier (see Fig. 6). However, one caveat should be added here: the identification and redshift for this source are uncertain (Paper I). Sources like this are very unusual, but do exist. One of the 7CRS galaxies, 5C7.178 at $z = 0.246$, is also ~ 2 magnitudes fainter than the mean $K - z$ relation (Willott et al. 2002b, 2003).

For both 6C**0935+4348 and 6C**1009+4327, the discrepancy between K-band magnitude and redshift suggests that the stellar content is not consistent with that of a massive host-galaxy. One possibility is that these sources are not yet fully formed (e.g. Jarvis, van Breukelen & Wilman 2005). If, as a consequence of the 'youth-redshift' degeneracy described by Blundell & Rawlings (1999), we are preferentially observing young sources ($\lesssim 10^7$ yr), then in some cases this could be the first instance of accretion activity in those sources. As such, this may trigger, or occur simultaneously with the initial star formation process in the host galaxy (e.g. Willott, Rawlings & Jarvis 2000; Willott et al. 2002a). If this is the case, it is perhaps not too surprising that their redshifts are overestimated by our method. As discussed by Willott et al. (2003), the best-fitting $K - z$ relation is close to the expected K-magnitude evolution of a galaxy of local luminosity 3 L_* which forms all of its stars in an instantaneous burst at $z_f = 10$.

However, 5C7.178, the 7CRS prominent outlier to the $K - z$ relation, is at low redshift and therefore unlikely to be a forming galaxy. This suggests that the 'young galaxy' hypothesis is not the only cause of underluminous outliers. The existence of a clear bright envelope to the K-z relation is presumably intimately related to the exponential cut-off in the galaxy Schechter function, whereas a tail to fainter magnitudes would be expected in any model in which powerful jets can, if only rarely, be associated with underluminous galaxies.

Apart from the objects so far discussed, the majority of sources have been assigned with a reasonably well-constrained redshift estimate, in that the true redshift lies within the 68 per cent confidence interval about the best-fitting redshift estimate. Our method seems therefore to be fairly robust whenever emission-line and/or non-stellar con-

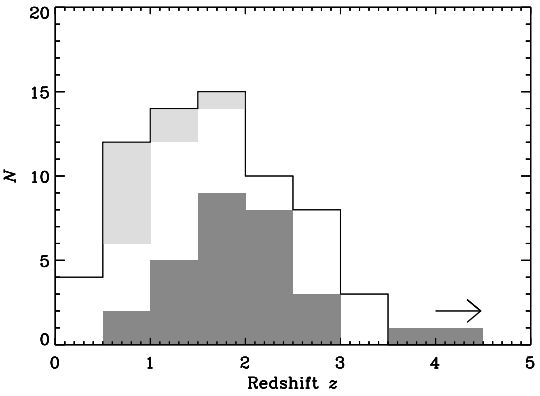

Figure 7. Estimated redshift distribution of the sources in the 6C** sample (solid line). The bin width is $\Delta z = 0.5$. The dark shadowed region is the distribution of sources in the 6C* sample (Jarvis et al. 2001b). The arrow above the $4.0 < z < 4.5$ bin represents the lower limit redshift estimates for 6C**0737+5618 and 6C**0935+4348. These are the two 6C** sources which are not detected in K-band (see also the caption of Table 2). The light shadowed region shows the locus of the nine quasars of which we know about in the 6C** sample (listed in table 9 of Paper I).

tributions to the K-band light can be neglected. However, we note that this could be a selection effect resulting from the spectroscopic incompleteness of the sample. Among the subsample of objects for which we do not have spectroscopic redshifts there could possibly be other sources like 6C**1009+4327 and 6C**0935+4348, that have redshift estimates significantly higher than their true redshifts.

We now compare the near-infrared Hubble diagram of the 6C** radio galaxies (for which we have a spectroscopic redshift) with the 3CRR, 6CE, 6C* and 7CRS samples (see Fig. 6). We find that the 6C** objects follow the same $K-z$ relation as the combined 3CRR/6CE/6C*/7CRS data, and have a rms dispersion of $\simeq 0.59$ mag over all redshifts if 6C**0935+4348 is excluded. This is consistent with the dispersion value used in our modelling (Section 2.2). If 6C**0935+4348, the prominent $K-z$ outlier, is included in this calculation, then the dispersion becomes $\simeq 0.75$ mag.

5 THE ESTIMATED REDSHIFT DISTRIBUTION

The estimated redshift distribution for the entire 6C** sample is presented in Fig 7. The median estimated redshift is $z \simeq 1.6$. It is informative to compare these results with the redshift distribution of the 6C* sample (Jarvis et al. 2001b) which, as mentioned before, has been filtered in a very similar way. The 6C* sample has a median redshift of $z \simeq 1.9$ and a redshift distribution skewed towards $z > 2$. This is a direct result of the filtering criteria applied to it.

Although the distribution of 6C** sources does have a tail to high redshift, the great majority of sources are at $z < 2$, in clear contrast to what should be expected. However, and in light of Section 4, we have to consider what is likely to be the major source of bias in our redshift estimation: the presence of quasars in the sample. These sources will be the ones which will be skewing the distribution the most towards lower redshifts. The redshift estimates of the three quasars with unresolved identifications (6C**0714+4616, 6C**0922+4216 and 6C**1036+4721), for which we have a spectroscopic redshift, are under-estimated by an average factor of 0.4. The major cause for concern is that there are quasars for which we do not have spectroscopic information. On the basis of K-band imaging alone, we assume that the further following sources are quasars (given that they have bright unresolved identifications; Paper I): 6C**0849+4658, 6C**1003+4827, 6C**1052+4349, 6C**1056+5730 and 6C**1138+3803. This leaves us with nine quasars[5], eight of which have redshift estimates in the range $0.5 < z \lesssim 1.0$. These alone represent a significant source of the bias towards low-redshift which we witness in Fig 7.

Removing the quasars from the distribution results in a median estimated redshift of $z \simeq 1.7$. This is similar to what is found for 6C* and much higher than the median redshift of similar, unfiltered samples (e.g. the 7CRS sample, at the same flux-density limit, with $z \approx 1.1$). This result confirms the efficiency of the filtering criteria, used for 6C**, in excluding low-redshift sources. Furthermore, we recall that some sources may also have their redshifts systematically under-estimated, due to emission-line contamination to their K-band magnitudes (Sections 3.2 and 4). Thus, it is quite plausible that the real redshift distribution has a slightly higher median redshift.

The fraction of quasars in the 6C** sample (9 quasars out of 68 objects) is higher than that in the 6C* sample. There are only two quasars out of the 29 6C* objects (Jarvis et al. 2001b). Although the difference is barely significant given the small numbers involved, it is possibly influenced by small differences in the selection criteria, such as the tighter size constraint or, more importantly, the lower frequency spectral index cut. For 6C*, the steep spectral index constrain is evaluated between 151 MHz and 4.85 GHz, thus excluding objects with prominent flat-spectrum cores, i.e. quasars. Because the 6C** spectral index cut goes up to only 1.4 GHz, this effect is less pronounced.

6 THE RLF MODEL OF STEEP-SPECTRUM RADIO SOURCES

Jarvis et al. (2001c) investigated the radio luminosity function for the most radio luminous low-frequency selected sources. The data used in their analysis were drawn from the complete 3CRR, 6CE and filtered 6C* samples by imposing a lower limit in radio luminosity. Only the sources which lie in the top-decade in $\log_{10} L_{151}$ were considered[6]. Focusing

[5] These include 6C**0928+4203, which does not appear unresolved in our near-infrared imaging, but shows broad emission lines in its spectrum (Paper I). We recall that this source has a redshift estimate which is in good agreement with its spectroscopic redshift (Section 4).

[6] This meant: $\log_{10} L_{151} \geq 27.63$ in their cosmology I ($\Omega_M = 1.0$, $\Omega_\Lambda = 0.0$, $H_0 = 50$ km s^{-1} Mpc^{-1}) and $\log_{10} L_{151} \geq 27.90$ in their cosmology II ($\Omega_M = 0.3$, $\Omega_\Lambda = 0.7$, $H_0 = 50$

on only the most luminous sources provided the largest possible baseline in redshift for the samples considered, while minimizing the role played (in the modelling procedure) by the intrinsic correlations between sample parameters, such as luminosity - spectral index and linear size - spectral index correlations, which are inherent to radio samples (Blundell, Rawlings & Willott 1999).

The filtered 6C* sample represented the greatest advance of this study over earlier work on the high-redshift RLF of low-frequency selected radio sources (Willott et al. 2001). However, its use required that the effects of the selection criteria, namely small angular size and steep radio spectral index, and in particular the fraction of sources which were missing from the survey, were taken into consideration in the modelling of the RLF. This led to a parameterisation which was separable in luminosity and redshift (as in Jarvis & Rawlings 2000 and in Willott et al. 2001), and also incorporated distributions in radio spectral shape and linear size, i.e.

$$\rho(L_{151}, z, a_1, a_2, D) = \rho_\circ \times \rho_L(L_{151}) \times \rho(z) \times \rho_a(a_1, a_2) \times \rho_D(D), \quad (8)$$

where $\rho_\circ$ is the normalising factor and a free parameter measured in units of Mpc^{-3}, $\rho_L(L_{151})$, $\rho(z)$, $\rho_a(a_1, a_2)$ and $\rho_D(D)$ are dimensionless distribution functions in radio luminosity, redshift, spectral shape parameters and projected linear size, respectively.

The full form of these distributions and their modelling are described in detail in Jarvis et al. (2001c). We now comment on the shape of the redshift distribution, for which Jarvis et al. (2001c) tested three different models. The model favoured by their maximum likelihood analysis (model C) uses a 1-tailed Gaussian to parameterise the low-redshift co-moving space density and a power-law distribution at high redshift, i.e

$$\rho_C(z) = \begin{cases} \exp\left\{-\frac{1}{2}\left(\frac{z-z_\circ}{z_1}\right)^2\right\} & : \quad z \le z_\circ \\ \left(\frac{1+z}{1+z_\circ}\right)^\eta & : \quad z > z_\circ, \end{cases} \quad (9)$$

where $z_\circ$ is the 'break' redshift where the model switches from the low- to the high-redshift form, z_1 is the characteristic width of the half-Gaussian and η is the power-law exponent describing the high-redshift co-moving space density. The other models tested by Jarvis et al. (2001c) were: model A – parameterised as a single Gaussian distribution in redshift; and, model B – a 1-tailed Gaussian which becomes constant and equal to unity beyond the Gaussian peak, i.e. the same as model C with η fixed at zero. The advantage of model C over the other models is that: (i) it breaks the symmetry between low- and high-redshift evolution which is forced by model A (and for which there is no physical basis), and (ii) allows for freedom in the evolution at high-redshift which is not possible with model B. Model C, is therefore more useful in terms of assessing the form of the evolution of the co-moving space density at high redshift.

Jarvis et al. (2001c) found a best-fitting power-law exponent $\eta = -0.06$ (in their Cosmology II), implying a constant co-moving space density beyond a peak redshift of $z_\circ = 2.15$ to an indeterminable redshift. A steep decline has been ruled out by their analysis at the $\sim 4\sigma$ level, but the form of the evolution at high redshift remained unresolved with an uncertainty encompassing both moderate declines and continuing shallow inclines.

km s^{-1} Mpc^{-1}), the two sets of cosmological parameters considered in their analysis.

7 COMPARISON WITH THE RLF OF STEEP-SPECTRUM RADIO SOURCES

To investigate the co-moving space density of high-redshift steep-spectrum radio sources, we now compare the redshift estimates derived from the 6C** data with the RLF of low-frequency selected radio sources of Jarvis et al. (2001c).

7.1 Selecting the most luminous 6C** sources

To be able to compare the 6C** data with the RLF model of Jarvis et al. (2001c), we must select the most radio luminous sources in the sample in a fashion that is equivalent to that of Jarvis et al. (2001c). For that we use the definition of top-decade in cosmology II of Jarvis et al. (2001c) and translate its lower radio luminosity limit to $\log_{10} L_{151} \ge 27.61$ in the cosmology used in this paper ($\Omega_M = 0.3$, $\Omega_\Lambda = 0.7$, $H_0 = 70$ km s^{-1} Mpc^{-1}). This means that, based strictly on the estimated $L_{151} - z$ diagram (Fig 8: top-panel), 12 of the 6C** sources are selected. However, if we consider also the spectroscopic redshifts available, i.e. by replacing estimated redshifts with spectroscopic ones where these are available (Fig 8: bottom-panel), then there are 17 sources in the top decade of radio luminosity. These sources are listed in Table 3, and include 6C**0737+5618. The inclusion of this source is discussed in more detail in Section 7.2.3. We note that two of the quasars with under-estimated redshifts (and luminosities) are now in the top-decade. A few of the quasars without spectra are also expected to move into the top-decade once their redshifts are known.

7.2 Analysis and discussion

We consider two ways of constructing the binned redshift distribution of 6C** sources in the top-decade of luminosity. In Section 7.2.2, we use spectroscopic redshifts when available, and otherwise the best-fitting redshift estimates, i.e. we consider the sources listed in Table 3 (see also Fig 8: bottom-panel). In Section 7.2.3, we take into account the redshift probability distribution of each source. Both redshift distributions are then compared with the expected redshift distribution given Jarvis et al. (2001c) model RLF.

7.2.1 The predicted redshift distribution

The predicted redshift distribution is obtained by integrating the model C RLF of Jarvis et al. (2001c), normalized to the sky area and evaluated for the radio selection criteria of the 6C** sample, i.e.

$$\frac{\mathrm{d}N}{\mathrm{d}z}(z) = \iiint \rho(L_{151},\, z,\, a_1,\, a_2,\, D) \times \Omega(L_{151},\, z,\, a_1,\, a_2,\, D) \times \frac{\mathrm{d}V}{\mathrm{d}z}\, \mathrm{d}(\log_{10} L_{151})\, \mathrm{d}a_1\, \mathrm{d}a_2\, \mathrm{d}(\log_{10} D) \quad (10)$$

Source name	Estimated $z_{\rm est}$	Estimated $\log_{10} L_{151}$	Spectroscopic $z_{\rm spec}$	Spectroscopic $\log_{10} L_{151}$	Cl.
6C**0737+5618	>4.0	>28.18			
6C**0744+3702	2.549	——	2.992	27.78	G
6C**0754+5019	3.331	27.97	2.996	27.85	G
6C**0801+4903	2.722	27.79			
6C**0824+5344	2.507	——	2.824	27.71	G
6C**0832+5443	2.240	——	3.341	27.69	G
6C**0902+3827	2.246	27.71			
6C**0909+4317	1.881	27.83			
6C**0922+4216	0.512	——	1.750	27.67	Q
6C**0925+4155	3.060	27.77			
6C**0928+4203	1.736	27.62	1.664	——	Q
6C**0935+4348	>4.0	>28.38	2.321	27.75	G
6C**1009+4327	3.089	28.42	1.956	27.91	G
6C**1036+4721	0.849	——	1.758	27.81	Q
6C**1045+4459	1.569	——	2.571	27.66	G
6C**1050+5440	2.773	27.79			
6C**1102+4329	2.732	27.78	2.734	27.79	G
6C**1103+5352	2.947	28.21			

Table 3. Sources selected from the 6C** sample which correspond to our top-decade definition (see Section 7.1). The rest-frame 151 MHz luminosities are in units of W Hz^{-1} sr^{-1} and were calculated assuming a simple power-law spectral index. The third column corresponds to a top-decade based strictly on the estimated redshift distribution. In this column the solid horizontal lines are used for sources which, based on their redshift estimates, fall below the lower luminosity limit. However, these sources are included in the top-decade if spectroscopic information (in columns 4–5) is taken into account. One source – 6C**0928+4203, is excluded. The classifications (G – radio galaxy; Q – quasar) are given only for sources which have optical spectroscopy (Paper I and references therein) and are based on these data.

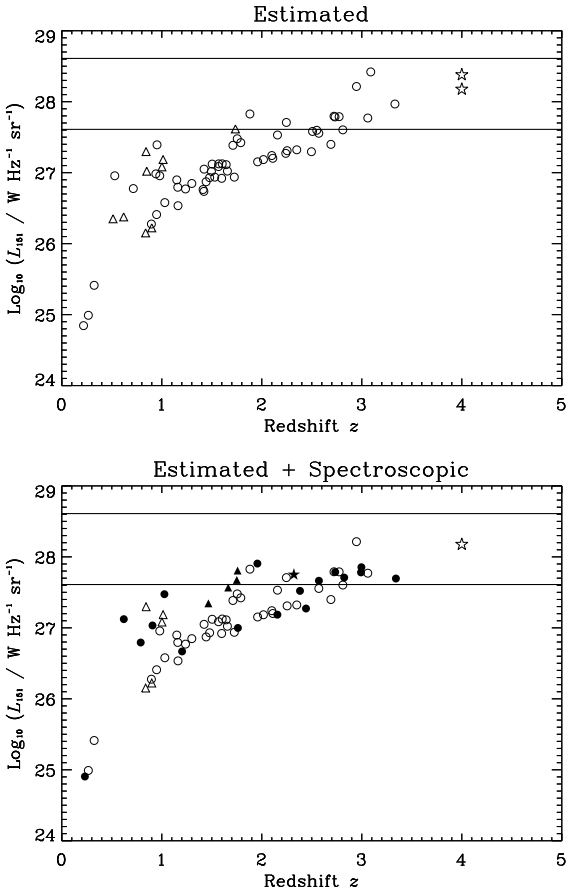

Figure 8. The estimated 151-MHz luminosity-redshift plane for the 6C** sample. The radio galaxies are represented by circles and the quasars by triangles. In the bottom-panel spectroscopic redshifts are taken into consideration (filled symbols). In both plots the star symbols represent the sources which were not detected in K-band (down to $K \simeq 21$ mag in an 8-arcsec aperture), i.e. 6C**0737+5618 and 6C**0935+4348. The area between the horizontal lines is the region which contains the 'most luminous' sources according to our definition, and which is equivalent to the top-decade in luminosity defined by Jarvis et al. (2001c). These plots are for $\Omega_M = 0.3$, $\Omega_\Lambda = 0.7$, $H_0 = 70$ km s^{-1} Mpc^{-1}.

where $\rho(L_{151}, z, a_1, a_2, D)$ is the complete radio luminosity function Jarvis et al. (2001c); $\Omega(L_{151}, z, a_1, a_2, D)$ is the sky area available for the 6C** sample; and, $({\rm d}V/{\rm d}z)$ is the differential co-moving volume element. The factor $\Omega(L_{151}, z, a_1, a_2, D)$ assumes a value of 0.421 sr (the sky area of 6C**) or zero, depending on whether or not a source with a given a set of the parameters L_{151}, z, a_1, a_2 and D meets the sample selecting criteria. The lower and upper limits of the integral are $27.61 \leq \log_{10} L_{151} \leq 28.61$, $-2.2 \leq a_1 \leq 1.0$, $-0.4 \leq a_2 \leq 0.2$ and $-0.3 \leq \log_{10} D \leq 4.0$. The integral was evaluated numerically, between $0 \leq z \leq 8$, using a Monte Carlo method, over 10^7 random points uniformly distributed in the 4-dimensional parameter space.

Because we use a different set of cosmological parameters than that of Jarvis et al. (2001c), we re-evaluated the luminosity function by using the relation from Peacock (1985):

$$\rho_1(L_1, z)\frac{{\rm d}V_1}{{\rm d}z} = \rho_1(L_2, z)\frac{{\rm d}V_2}{{\rm d}z} \qquad (11)$$

where ρ_1 and ρ_2 are the luminosity functions for two different cosmologies, and, L_1 and L_2 are the luminosities derived from the flux density, redshift and proper motion distance in each of the two different cosmologies. We used the RLF model evaluated in Cosmology II of Jarvis et al. (2001c) to obtain the RLF used in Eq. 10.

The best-fitting parameter $\log_{10} D_o$, the peak of the Gaussian distribution in $\log_{10}$ of the projected linear size D (eq. 7 of Jarvis et al. 2001c), was also redefined due to the change in the set of cosmological parameters used. Since this is just a change in the Hubble constant, the relation between the linear sizes in the two cosmologies is then simply proportional to the ratio of their respective Hubble constants. For model C, $\log_{10} D_o$ becomes 1.97 in the cosmology used in this paper. All the other parameters remained the same (table 3 of Jarvis et al. 2001c).

7.2.2 Using the best-fitting redshift estimates

The redshift distribution of 6C** sources in the top-decade of luminosity, based on their best-fitting redshift estimates ($z_{\rm est}$) and on the spectroscopic redshifts available, is shown in Fig. 9. In general, the model redshift distribution is a fairly good approximation to the data. There is excellent agreement at $z < 2$, and it is also apparent that: (i) there is

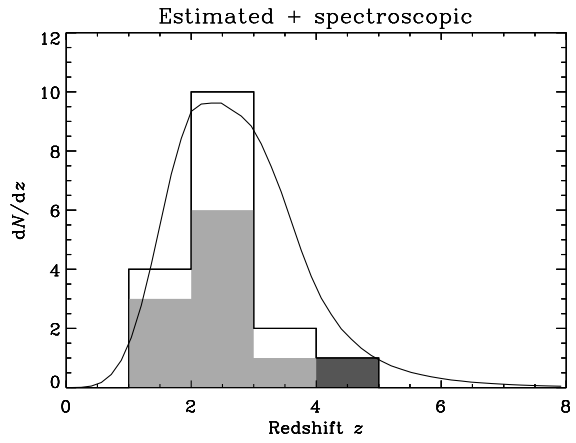

Figure 9. The histogram shows the number of sources in the 6C** sample with $\log_{10} L_{151} \geq 27.61$, drawn from the 'estimated + spectroscopic' $L_{151} - z$ diagram (Fig. 8: bottom-panel), binned in redshift with bin width $\Delta z = 1$. The light shaded region represents the sources which have spectroscopic redshifts. The solid line shows Jarvis et al. (2001c) model C predictions ($\eta = -0.06$, constant co-moving space density) for the redshift distribution (Section 7.2.1). The dark shaded region represents 6C**0737+5618, for which the redshift estimate is a lower limit based on extrapolation of the $K - z$ relation (see also the caption of Table 2).

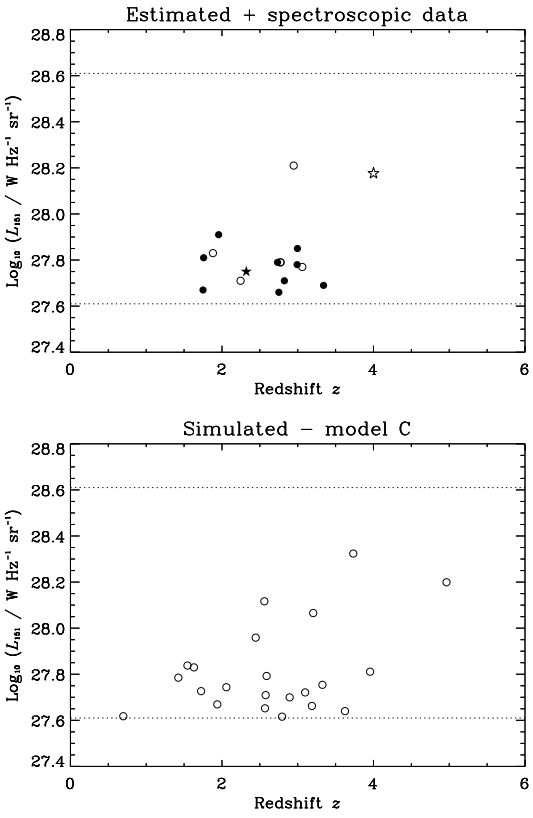

Figure 10. The top panel shows the estimated top-decade (delimited by the dotted horizontal lines) of the $L_{151} - z$ plane for the 6C** sample. The spectroscopic redshifts are included (by replacing estimated redshifts with spectroscopic ones when these are available), and are represented by the filled symbols. The star symbol represents 6C**0737+5618. The bottom panel shows a simulation of the top-decade of the $L_{151} - z$ plane for a sample with the same flux limit, sky area and radio selection criteria as 6C**. This simulation was generated using the best-fitting model C of Jarvis et al. (2001c), translated to our adopted cosmology.

a slight deficit of sources predicted at $2 < z < 3$; and, (ii) there is an excess of predicted sources at $z > 3$. However, we note that it is at these redshifts that the effects of the small number statistics become more important. Moreover, our redshift estimation method relies on the limited statistics of the 3CRR, 6CE, 7CRS and 6C* radio galaxies at $z > 3$, where the scatter in the $K-z$ diagram is still poorly defined.

Similar comments can be made when we use the RLF model to create an artificial $L_{151} - z$ plane and compare it with the one estimated from the data, including the spectroscopic redshifts (Fig. 10). In general, it is apparent that the model predicts more sources (22) than the ones that are present in the estimated+spectroscopic diagram (17 sources). However, we caution that, since both the estimated data and the simulations have independent Poisson errors, this comparison can only be regarded in a qualitative way.

To explore the significance of these results, we apply the Kolmogorov-Smirnov test to compare the redshift distribution derived from data and the predicted model distribution (Fig. 9). We find that they are not significantly different, with probability $p = 0.29$. Thus, we can conclude that the data are consistent with Model C of Jarvis et al. (2001c), the constant co-moving space density model.

7.2.3 Taking the redshift probability distributions into account

We now construct the redshift distribution of the top-decade sources by taking into account the redshift probability distribution of each source (derived from the $K - z$ diagram), rather than just using the best-fitting redshift estimate. In practice, since the probability density functions (derived in Section 2.3) are normalised to unity, when the binned redshift distribution is constructed each source contributes to a number of redshift bins, with an amount proportional to the probability of the source lying within that bin. For each source, we calculate also the redshift which corresponds to a luminosity of $\log_{10} L_{151} \geq 27.61$, which is the lower limit of the top-decade, and only take into account contributions which lie above that redshift. All the sources are considered, i.e. we include also those sources whose best-fitting redshift estimate would put them below the lower-limit of the top-decade in luminosity, and consider the contribution from the high-redshift tail of their probability distributions. The spectroscopic redshifts, when available, are also taken into consideration. The sources with spectroscopic redshifts contribute to a single bin each, if their luminosity lies above the lower limit of the top-decade (see Table 3). 6C**0737+5618, the source which is not detected in K-band and does not have a spectroscopic redshift, contributes also to a single bin ($4 < z < 5$). The resulting redshift distribution is presented in Fig. 11.

The distribution derived from the data appears to be in very good agreement with the model distribution. This is confirmed by the application of the chi-squared goodness-

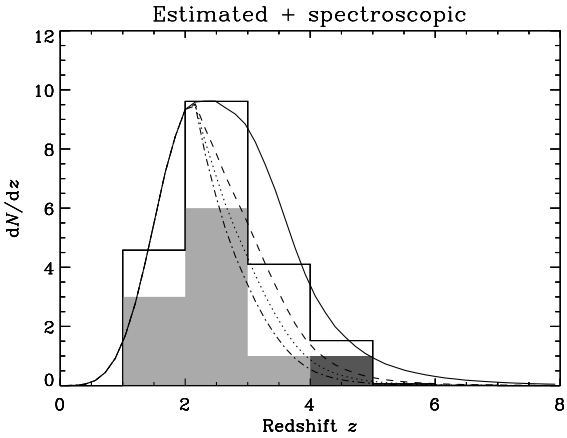

Figure 11. The binned redshift distribution of sources in the top-decade (i.e. with $\log_{10} L_{151} \geq 27.61$), constructed by taking the redshift probability density functions of Section 2.3 into account, rather than just the best-fitting redshift estimates (see Fig 9), as described in Section 7.2.3. The bin width is $\Delta z = 1$. Each source contributes to a number of bins, with an amount proportional to the probability of the source lying within that bin. The available spectroscopic redshifts are also taken into consideration. These contribute to a single bin each and are represented by the light shaded region. The solid line shows Jarvis et al. (2001c) model C predictions ($\eta = -0.06$, constant co-moving space density) for the redshift distribution (Section 7.2.1). The dashed, dotted and dot-dashed lines show the same model predictions but for declining co-moving space densities with $\eta = -2.0$, $\eta = -3.0$ and $\eta = -4.0$, respectively. The dark shaded region represents 6C**0737+5618, for which the redshift estimate is obtained based on extrapolation of the $K - z$ relation, and a probability density function was not derived (see also the caption of Table 2). This source contributes to a single bin, the $4 < z < 5$ bin.

of-fit test, which gives $\chi^2 = 1.2$, with a probability $p = 0.54$ of obtaining this, or greater than this value of χ^2.

We perform also the same analysis by omitting 6C**0737+5618 in the $4 \leq z \leq 5$ bin. This source is unidentified and it is debatable that its K-band magnitude limit ($K \gtrsim 21$ mag in a 8-arcsec aperture at the 3σ level) implies, by extrapolation of the $K - z$ diagram, a very high redshift ($z > 4$). It is also possible that this source, like 6C**0935+4348, is at a lower redshift ($z \simeq 2 - 3$) but is perhaps at a very early stage of its formation and/or highly obscured, or is simply underluminous (see discussion in Section 4). However, a very high-redshift cannot be ruled out.

Omitting 6C**0737+5618 from our analysis does not change the results significantly. We find $\chi^2 = 2.4$, with $p = 0.36$. Again, we conclude that the data are consistent with the constant co-moving space density model of Jarvis et al. (2001c).

Finally, we compare the data with the predictions from five declining co-moving space density models, using Jarvis et al. (2001c) model C with: $\eta = -2.0$ (dashed line in Fig. 11), $\eta = -2.5$, $\eta = -3.0$ (dotted line in Fig. 11), $\eta = -3.5$ and $\eta = -4.0$ (dot-dashed line in Fig. 11). The results of the chi-squared goodness-of-fit test are listed in Table 4. It can be seen that, although the data are also consistent with moderate declines by factors of 2 to 3, declines by a factor of 3.5 and 4.0 can be excluded at the $\sim 2 - 3\sigma$ level.

			Omitting 6C**0737+5618		Notes
η	χ^2	p	χ^2	p	
-0.06	1.2	0.54	2.4	0.36	constant space density
-2.0	1.4	0.24	0.8	0.36	declining space density
-2.5	2.4	0.12	1.6	0.21	declining space density
-3.0	3.7	0.05	2.6	0.11	declining space density
-3.5	5.2	0.02	3.8	0.05	declining space density
-4.0	6.8	0.009	5.1	0.02	declining space density

Table 4. The results of the chi-squared goodness-of-fit test to compare the model and data redshift distributions of Fig. 11. The first column lists the value of the parameter η, which is the power-law exponent describing the high-redshift co-moving space density (see Eq. 9). Columns two and three give the values of chi-square χ^2, and the probability p of obtaining that value of χ^2 or greater, when including 6C**0737+5618 in the analysis. Columns four and five list the same values, when omitting this source.

7.2.4 The limitations of a filtered sample

As discussed by Jarvis (2000), filtered samples such as 6C** have limitations when it comes to confirming a decline in co-moving space density. The major problem is that the lack of sources at a given redshift may not be due to a decline in their space density but to imperfections in the filtering technique. For example, with respect to the 6C* sample, Jarvis (2000) estimated that the angular size selection is filtering out an increasingly large fraction of the sources with redshift: from $\sim 20\%$ to $\sim 30\%$ between $z = 0$ and $z \sim 5$; and $\sim 30 - 50\%$ beyond $z > 5$. Jarvis (2000) concluded that samples with similar filtering criteria to that of 6C*, and in particular with flux-density limits similar to that of 6C**, are only able to confirm roughly constant or increasing co-moving space density at high redshifts. The presence of a decline would be difficult to interpret due to the uncertainties introduced by the filtering criteria. However, the filtering is helpful in placing strong lower limits on any decline.

8 SUMMARY

A method of redshift estimation, based on the $K - z$ diagram of the 3CRR, 6CE, 6C* and 7CRS radio galaxies has been developed. Redshift probability density functions are derived for all of the 6C** sources which are identified with a near-infrared counterpart, i.e. for 66 of the 68 members of the sample. Comparison of the resulting redshift estimates with the subset of spectroscopic redshifts shows that our method is fairly robust whenever emission-line and/or non-stellar contributions to the K-magnitudes can be neglected. The estimated redshift distribution has a median redshift of $z_{\rm med} \simeq 1.6$. However, we find that the quasars have their redshifts significantly under-estimated by our method. This is explained by the fact that the method is based on the $K-z$ relation, which is only valid for radio galaxies. Removing the quasars from the distribution results in a median estimated

redshift of $z \approx 1.7$. This is similar to that of the 6C* sample ($z_{\rm med} \approx 1.9$) and is significantly higher than that of unfiltered, complete surveys at the same flux density limit. We conclude that the filtering criteria were effective in biasing the 6C** sample to objects at high-redshift.

The redshift distribution of the most luminous sources in the 6C** sample is compared with the predictions of the steep-spectrum RLF model of Jarvis et al. (2001c). We find that the 6C** data is consistent with a constant co-moving space density at $z \gtrsim 2.5$, and moderate declines by factors of ~ 4 can be excluded at the $\sim 2-3\sigma$ level. Although Jarvis et al. (2001c) excluded these declines at the $\sim 4\sigma$ level, the additional data from 6C** provide an independent measure. Thus, the two independent studies are in quantitative agreement with the result that any decline at high redshift is shallow.

We note that our result is based on a redshift distribution which is uncertain for the following reasons: (i) a significant fraction of the sample is not identified spectroscopically; (ii) the method of redshift estimation relies on the limited statistics of the 3CRR, 6CE, 7CRS and 6C* radio galaxies at $z > 3$ (the scatter in the $K-z$ diagram at these high redshifts is still poorly defined); and (iii) the redshift estimates of quasars are systematically under-estimated by our method. Most of these are likely to lead to an underestimate of the true median redshift of the complete sample. Thus, although spectroscopically incomplete, with the 6C** sample we have additional strong constraints on the high-redshift space density, with a sample that increases the number of powerful steep-spectrum sources, from complete samples at $z > 2$, by a factor of ~ 2.

The work presented here could be significantly improved by obtaining spectroscopic redshifts for a larger fraction of sources in the 6C** sample. This would be particularly important for the faintest sources ($K \gtrsim 19$ mag), since these are the most probable $z > 2$ candidates. With spectra of these sources we should be able to obtain a tighter constrain on the co-moving space density at $z > 2$.

ACKNOWLEDGEMENTS

We thank Isobel Hook and Ross McLure for very useful comments. MJC acknowledges the support from the Portuguese Fundação para a Ciência e a Tecnologia, and the receipt of a NOVA Marie Curie Early Stage Training Fellowship. She also gratefully acknowledges the generous hospitality of the Institute for Computational Cosmology and the Extragalactic Cosmology Research Group, at Durham University. KMB acknowledges the Royal Society for a University Research Fellowship.

REFERENCES

Allington-Smith J. R., Lilly S. J., Longair M. S., 1985, Mon. Not. R. Astr. Soc., 213, 243
Blundell K. M., Rawlings S., 1999, Nature, 399, 330
Blundell K. M., Rawlings S., Eales S. A., Taylor G. B., Bradley A. D., 1998, Mon. Not. R. Astr. Soc., 295, 265
Blundell K. M., Rawlings S., Willott C. J., 1999, Astron. J., 117, 677
Bower R. G., Benson A. J., Malbon R., Helly J. C., Frenk C. S., Baugh C. M., Cole S., Lacey C. G., 2006, Mon. Not. R. Astr. Soc., 370, 645
Brinkmann W., Laurent-Muehleisen S. A., Voges W., Siebert J., Becker R. H., Brotherton M. S., White R. L., Gregg M. D., 2000, Astron. Astrophys., 356, 445
De Breuck C., van Breugel W., Röttgering H., Stern D., Miley G., de Vries W., Stanford S. A., Kurk J., Overzier R., 2001, Astron. J., 121, 1241
De Breuck C., van Breugel W., Stanford S. A., Röttgering H., Miley G., Stern D., 2002, Astron. J., 123, 637
Cruz M. J. et al., 2006, MNRAS, 373, 1531 (Paper I)
Dunlop J. S., McLure R. J., Kukula M. J., Baum S. A., O'Dea C. P., Hughes D. H., 2003, Mon. Not. R. Astr. Soc., 340, 1095
Dunlop J. S., Peacock J. A., 1990, Mon. Not. R. Astr. Soc., 247, 19
Eales S., Rawlings S., Law-Green D., Cotter G., Lacy M., 1997, Mon. Not. R. Astr. Soc., 291, 593
Eales S. A., Rawlings S., 1993, Astrophys. J., 411, 67
Eales S. A., Rawlings S., 1996, Astrophys. J., 460, 68
Fan X., Strauss M. A., Schneider D. P., Becker R. H., White R. L., Haiman Z., Gregg M., Pentericci L. et al., 2003, Astron. J., 125, 1649
Hales S. E. G., Baldwin J. E., Warner P. J., 1988, Mon. Not. R. Astr. Soc., 234, 919
Hales S. E. G., Masson C. R., Warner P. J., Baldwin J. E., 1990, Mon. Not. R. Astr. Soc., 246, 256
Jarvis M. J., 2000, PhD thesis, University of Oxford
Jarvis M. J., Rawlings 2000, Mon. Not. R. Astr. Soc., 319, 121
Jarvis M. J., Rawlings S., Eales S., Blundell K. M., Bunker A. J., Croft S., McLure R. J., Willott C. J., 2001a, Mon. Not. R. Astr. Soc., 326, 1585
Jarvis M. J., Rawlings S., Lacy M., Blundell K. M., Bunker A. J., Eales S., Saunders R., Spinrad H., Stern D., Willott C. J., 2001b, Mon. Not. R. Astr. Soc., 326, 1563
Jarvis M. J., Rawlings S., Willott C. J., Blundell K. M., Eales S., Lacy M., 2001c, Mon. Not. R. Astr. Soc., 327, 907
Jarvis M. J., van Breukelen C., Wilman R. J., 2005, Mon. Not. R. Astr. Soc., 358, L11
Lacy M., Bunker A. J., Ridgway S. E., 2000, Astron. J., 120, 68
Laing R. A., Riley J. M., Longair M. S., 1983, Mon. Not. R. Astr. Soc., 204, 151
Lilly S. J., Longair M. S., 1984, Mon. Not. R. Astr. Soc., 211, 833
Longair M. S., 1966, Mon. Not. R. Astr. Soc., 133, 421
Marshall H. L., Tananbaum H., Avni Y., Zamorani G., 1983, Astrophys. J., 269, 35
McCarthy P. J., 1991, Astron. J., 102, 518
McCarthy P. J., 1993, Ann. Rev. Astron. Astrophys., 31, 639
McLure R. J., Jarvis M. J., 2004, Mon. Not. R. Astr. Soc., 353, L45
McLure R. J., Willott C. J., Jarvis M. J., Rawlings S., Hill G. J., Mitchell E., Dunlop J. S., Wold M., 2004, Mon. Not. R. Astr. Soc., 351, 347
Night C., Nagamine K., Springel V., Hernquist L., 2006, Mon. Not. R. Astr. Soc., 366, 705
Peacock J. A., 1985, Mon. Not. R. Astr. Soc., 217, 601
Rawlings S., Eales S., Lacy M., 2001, Mon. Not. R. Astr. Soc., 322, 523
Shaver P. A., Wall J. V., Kellermann K. I., Jackson C. A., Hawkins M. R. S., 1996, Nature, 384, 439
van Breugel W., De Breuck C., Stanford S. A., Stern D., Röttgering H., Miley G., 1999, Astrophys. J. Lett., 518, L61
Vigotti M., Vettolani G., Merighi R., Lahulla J. F., Lopez-Arroyo M., 1990, Astron. Astrophys. Suppl., 83, 205
Wall J. V., Jackson C. A., Shaver P. A., Hook I. M., Kellermann K. I., 2005, Astron. Astrophys., 434, 133
Willott C. J., 2001, in EAS Publications Series, Volume 1. Active galactic nuclei in their cosmic environment. Ed. by B. Rocca-

Volmerange and H. Sol. Radio-optical correlations in high-z radio galaxies and quasars. pp 109–118
Willott C. J., Rawlings S., Archibald E. N., Dunlop J. S., 2002a, Mon. Not. R. Astr. Soc., 331, 435
Willott C. J., Rawlings S., Blundell K. M., Lacy M., Eales S. E., 2001, Mon. Not. R. Astr. Soc., 322, 536
Willott C. J., Rawlings S., Blundell K. M., Lacy M., Hill G. J., Scott S. E., 2002b, Mon. Not. R. Astr. Soc., 335, 1120
Willott C. J., Rawlings S., Jarvis M. J., 2000, Mon. Not. R. Astr. Soc., 313, 237
Willott C. J., Rawlings S., Jarvis M. J., Blundell K. M., 2003, Mon. Not. R. Astr. Soc., 339, 173
Zirm A. W., Dickinson M., Dey A., 2003, Astrophys. J., 585, 90